



# Electron beam welding of rolled and laser powder bed fused Inconel 718

Akash Sali<sup>1</sup> · Vivek Patel<sup>1</sup> · James Hyder<sup>2</sup> · David Hyder<sup>2</sup> · Mike Corliss<sup>2</sup> · Wayne Hung<sup>1</sup> 

Received: 17 October 2021 / Accepted: 14 March 2022 / Published online: 31 March 2022  
© The Author(s), under exclusive licence to Springer-Verlag London Ltd., part of Springer Nature 2022

## Abstract

This paper explores the feasibility of welding Inconel 718 (IN718) and compares the quality of electron beam welded samples produced by hot rolling and laser powder bed fusing (L-PBF). Electron beam heat input, varying in the range 175–300 J/mm, was the main parameter in welding. Microhardness, tensile properties, and fractography study using both optical and scanning electron microscopy were employed to analyze and compare the quality of the welded samples. Energy-dispersive X-ray analysis was used to identify chemical compositions of different phases on the fractured surfaces. Large voids were observed at high heat inputs ( $\geq 213$  J/mm). Excellent weld penetration was obtained and was proportional to the beam heat input. Both yield and tensile strength of the welded L-PBF materials exceeded those of rolled materials and met the minimum requirement from ASTM specification; however, the ductility of welded L-PBF material did not. The brittleness of these L-PBF materials came from the brittle Laves phase and Al-Ti-O compounds in the microstructure and non-optimal L-PBF parameters. These drawbacks can be further reduced by adjusting the L-PBF parameters and suitable post-processing techniques before electron beam welding.

**Keywords** Laser powder bed fusion · Electron beam welding · Inconel 718 · Rolling

## Abbreviations

ASM American Society for Metals  
ASTM American Society for Testing and Materials  
DA Dual aging  
DAZ Diffusion affected zone  
EBW Electron beam welding  
EDM Electrical discharge machining  
EDS Energy-dispersive spectroscopy

FZ Fusion zone  
HAZ Heat affected zone  
HV Vickers hardness  
HIP Hot isostatic pressing  
IN718 Inconel 718  
ISZ Isothermally solidified zone  
L-PBF Laser powder bed fusion  
PT Precipitation treatment  
SEM Scanning electron microscopy  
SLM Selective laser melting  
SR Stress relieve  
ST Solution treatment  
TIG Tungsten inert gas welding  
UTS Ultimate tensile strength  
YS Yield strength  
 $\epsilon$  Elongation (%)

✉ Wayne Hung  
hung@tamu.edu

Akash Sali  
saliakash048@tamu.edu

Vivek Patel  
vivekpatel@tamu.edu

James Hyder  
jhyder@kgsbo.com

David Hyder  
dhyder@kgsbo.com

Mike Corliss  
mcorliss@kgsbo.com

<sup>1</sup> Texas A&M University, College Station, TX 77843, USA

<sup>2</sup> Knust-Godwin LLC, Katy, TX 77494, USA

## 1 Introduction

Selective laser melting (SLM) is a laser-based powder bed fusion (L-PBF) process in which parts are built layer-by-layer with atomized metal powder. The L-PBF process can produce near-net-shaped parts with minimal material

wastage as compared to conventional subtractive manufacturing processes. This unconventional method of producing parts provides greater geometrical flexibility to their designs with fewer constraints on manufacturability. It has exceeded from being a mere rapid prototyping technique to a method of manufacturing components that can be used in actual engineering applications. Despite the advantages of the L-PBF process, final dimensions of L-PBF parts are limited to the chamber sizes of available powder bed fusion machines. Consequently, current L-PBF machines are insufficient to produce large and complex shaped components desired by various industries such as aerospace, defense, automotive, nuclear, and energy. Thus, the development of efficient ways to join the smaller components is necessary to utilize additive manufacturing to its full potential.

Inconel 718 (IN718) superalloy is widely used in the above-mentioned industries. This is due to its superior mechanical properties such as tensile strength, hardness, creep resistance, and corrosion resistance even at temperatures as high as 650 °C [1]. Given their stable grain structure and strain hardening properties, it is expensive to execute complex machining operations on the conventionally manufactured IN718 parts [2]. Thus, L-PBF of IN718 has gained popularity to produce intricate parts. Welding of IN718 also comes with its challenges and thus has been explored widely by various researchers. Among all the welding processes, electron beam welding (EBW) could provide excellent results in terms of weld quality, excellent weld penetration, and weld strength [3]. It also exerts less thermal stress on the base metal thereby imposing minimal metallurgical and microstructural changes. This research study is motivated by the need for high quality and large additive manufactured parts and a lack of published literature for EBW of L-PBF IN718. The objectives of this study were to:

1. Explore the feasibility of joining additively manufactured IN718
2. Compare the quality of rolled and powder-bed fused IN718 after welding with electron beam

## 2 Literature review

### 2.1 Joining methods for rolled IN718

Laser welding was investigated for joining of rolled IN718 parts [4]. The authors used 5-mm-thick rolled plates with two different grain structures (fine and coarse) for welding with CO<sub>2</sub> laser at powers ranging from 5 to 10 kW with

helium (15 L/min) as the shielding gas. The samples were pre-weld heat-treated at two different conditions. A full penetration weld with no spatter, cracks, or porosity was observed at a lower power of 6 kW and mid-range welding speeds of 2–3 m/min. Higher laser powers did give full penetration welds but produced undesirable defects. Fine-grained samples had relatively fewer defects and less segregation of alloying elements. Pre-weld treated samples performed poorly due to the segregation of niobium after heat treatment. Post-weld heat-treating of the samples provided better results with ultimate tensile strength (UTS) of 1380 MPa, yield strength (YS) of 1253 MPa, and elongation at fracture (%  $\epsilon$ ) of 4% as compared to the respective values of 1380 MPa, 1068 MPa, and 18% for the base metal. This was due to the liquation of heat affected zone (HAZ) micro-fissures induced in the welding process, and precipitation of the delta phase  $\delta$  at grain boundaries.

Electron beam welding has been widely explored for wrought IN718. Many variations in process parameters and heat treatments have led to efficient welding of IN718 by EBW. In one research [5], the effect of pre-weld heat treatment conditions on HAZ was explored using hardness test data and microstructural analysis. The 3-mm-thick samples treated at two different conditions (solution treatment (ST) at 950°/1 h/water quenching and ST + precipitation treatment (PT) at 760 °C/1 h/ water quenching) were welded using two weld passes. The ST + PT samples showed a spike in hardness values from 260 HV at the weld zone to 370 HV at HAZ boundary due to its high thermal sensitivity and the precipitation of  $\gamma'$  and  $\gamma''$  phases in HAZ. Scanning electron microscopy (SEM) was utilized to identify HAZ of as-received and ST samples since they were not distinguishable by microhardness measurement.

Elliptical oscillations of electron beam during the welding process was shown to improve material characteristics and the mechanical properties of 3.1-mm thick-IN718 welds [6]. Welded samples were also subjected to two heat treatments. Oscillation welded samples treated at 980 °C ST+PT gave the best results with 1220 MPa YS, 1390 MPa UTS, and 20% elongation as compared to 1035 MPa, 1200 MPa, and 12%, respectively, for unoscillated samples. Hardness values improved from 495 HV for unoscillated to 520 HV for oscillated samples. Thus, better cooling rates, high fluid flow due to lower viscosity, and reduced thermal gradients in the weld pools induced by beam oscillations had a positive impact on reducing Nb segregation and Laves phase formation. The heat input from an energy beam, either laser or electron beam, is defined by Eq. (1). Heat input (or thermal energy density) had a significant influence on the formation of HAZ micro-fissures on IN718 material [7].

$$\text{Heat input} \left( \frac{\text{J}}{\text{mm}^3} \right) = \frac{\text{Beam current (A)} \times \text{Beam voltage (V)}}{\text{Layer thickness (mm)} \times \text{Hatch distance (mm)} \times \text{Welding speed} \left( \frac{\text{mm}}{\text{s}} \right)} \quad (1)$$

When layer thickness and hatch distance were kept constant, then Eq. (1) had a simpler form:

$$\text{Heat input} \left( \frac{\text{J}}{\text{mm}} \right) = \frac{\text{Beam current (A)} \times \text{Beam voltage (V)}}{\text{Welding speed} \left( \frac{\text{mm}}{\text{s}} \right)} \quad (2)$$

Lower heat input in the vicinity of 36 J/mm induced higher temperature gradients in HAZ and thus produced larger grain boundary areas for cracking. A general increase in the weld width from 2.0 to 3.5 mm was observed as the heat input increased from 40 to 180 J/mm owing to the higher melting of metal at higher beam currents. Other research investigated the effect of variation in welding speed and base metal condition of rolled IN718 [8]. Laves phase formation increased due to higher micro-segregation at the weld center as the welding speed was increased. Both the base metal condition or pre-weld heat treatment and welding speed had a significant impact on HAZ micro-fissures. The HAZ cracking increased with increasing temperature of pre-weld heat treatments and welding speed.

The 12-mm-thick EBW penetration was achieved on rolled IN718 plates using two weld passes; the first was with a high beam current of 120 mA, and the second was with a low beam current of 30 mA [9]. Samples were also heat-treated after welding by ST at 980 °C/1 h/air cooling and dual aging (DA) 720 °C/8 h/furnace cooling at 50 °C/h + 620 °C/8 h/air cooling. Mechanical properties measured at the top, middle, and bottom sections of the 12 mm weld indicated improvement in mechanical properties towards the bottom of the weld. Perhaps this was due to a gradual reduction in the weld grain size towards the bottom of the weld. The high temperature tensile mechanical properties in all three regions were still less than the base metal. Due to the reduction in precipitation of hardening phases in the fusion zone (FZ), hardness was lesser as compared to the base metal region.

The EBW was successfully utilized to join 13-mm-thick rolled IN718 plates [10]. Weld area and penetration depth

increased with an increase in heat input. Although, keyhole defects were observed at a high heat input power of 3250 W. Samples welded at low heat inputs exhibited higher tensile strength that exceeded base material specification (837 MPa) and fractured outside the weld with typical elongation of 57%. While those samples that welded at a higher heat input fractured at the welds.

## 2.2 Joining methods for L-PBF components

Published literature showed results of tungsten inert gas (TIG) welding and brazing for L-PBF IN718, laser welding and EBW for L-PBF parts of other materials. Residual stresses and inevitable development of pores due to lack of fusion or non-uniform shrinkage in L-PBF parts were some of the factors that contributed to inferior material properties as compared to those manufactured by conventional methods. Layer-wise build-up, localized heating /cooling cycles, and quick solidification of molten metal along the laser path during an L-PBF process contributed to these issues [11]. These factors also gave anisotropic properties to L-PBF parts. The orientation, in which the samples were built, significantly affected their tensile properties. The L-PBF IN718 parts exhibited inferior YS and UTS but better ductility in their building direction as compared to the other directions. This was due to the difference in orientation of crystal structure, residual stresses, and accumulation of dislocations in the loading direction relative to the building direction. The positive effect of various heat treatments on YS, UTS, and hardness of L-PBF IN718 parts was also observed. Elongation at fracture decreased in heat-treated samples and confirmed in another research that associated anisotropic behavior of mechanical properties in L-PBF parts to the number of layers along the loading direction and homogeneity of the alloy leading to inferior  $\gamma'$  phase distribution [12]. The results of this research are summarized in Table 1. However, a rise in microhardness values was observed due to the dissolution of Laves into the  $\gamma$  matrix after homogenization and stress relieving heat treatments [13].

**Table 1** Anisotropic properties of L-PBF IN718 [12]

Sample condition	Sample orientation	UTS (MPa)	0.2% YS (MPa)	Fracture strain (%)	Vickers hardness (HV)
As-built	Horizontal	1085 ± 11	816 ± 24	19.1 ± 0.7	341
	Vertical	1010 ± 10	737 ± 4	20.6 ± 2.1	307
HT1 <sup>a</sup>	Horizontal	1447 ± 10	1227 ± 1	10.1 ± 0.6	452
	Vertical	1357 ± 5	1136 ± 16	13.6 ± 0.2	453
HT2 <sup>b</sup>	Horizontal	1471 ± 4	1222 ± 26	15.9 ± 1.0	439
	Vertical	1387 ± 12	1186 ± 23	17.4 ± 0.4	448

<sup>a</sup>Solution treatment at 980 °C/1 h/air cooling, followed by dual aging at 720 °C/10 h/furnace cooling for 2 h to 650 °C + 620 °C/8 h

<sup>b</sup>Homogenization at 1065 °C/1 h followed by HT1 process

The HAZ micro-fissures were observed in TIG welds of as-built and hot isostatic pressed (HIP) L-PBF IN718 samples after varestreint tests [14]. It was observed that the HIP samples had the highest susceptibility to cracks due to the formation of larger grain boundaries causing higher stress concentration and providing crack initiation sites. The as-built L-PBF samples had the same crack lengths as compared to their wrought IN718 counterparts. Brazing was explored as a potential way to join L-PBF IN718 parts with a BNi-2 filler metal in another research [15]. Isothermally solidified zone (ISZ) surrounded by diffusion affected zone (DAZ) was formed at the brazing joint. The ISZ had a slightly lower hardness (460HV) as compared to the DAZ (485 HV) and the base metal (470 HV). The brazed joint had a shear strength of 802 MPa which was about 77% of the base metal strength.

Electron beam welding was applied to join cylindrical L-PBF AlSi10Mg alloy parts [16]. Heat inputs in the range from 21 to 58 J/mm were explored in this research. The overall geometry of the weld was strongly influenced by the EBW heat input while the weld penetration was mainly affected by the welding speed and beam current. Deeper welds were achieved at high speeds and high beam currents individually. However, high speeds also induced higher porosity in the fusion zone. The fusion zone had a slightly lower hardness of 103 HV in general as compared to the base metal hardness of 111 HV. Another research explored laser welding to join 5-mm-thick L-PBF titanium alloy Ti-6Al-4V at 4 kW laser power and speed ranging from 1.0 to 2.5 m/min [17]. Full penetration weld without cracks was achieved for all the samples; however, pores were observed in all the samples. The weld zone had higher hardness as compared to HAZ and base metal. Heat treatments (850 °C/2 h/furnace cooling) reduced hardness by ~30HV and tensile properties by ~100 MPa of L-PBF base metal and the welds. Laser-arc hybrid welding was successfully implemented for welding of L-PBF 316L stainless steel parts [18]. Tensile tests revealed on par mechanical strength of welded L-PBF samples as compared to the rolled samples although the ductility of L-PBF samples was inferior (2.5 mm for L-PBF sample against 5.72 for wrought sample). The hardness of the fusion zone was greater than the wrought sample and less than the L-PBF samples. Similar results for hardness were obtained for friction welded aluminum alloy Al-12Si parts

manufactured by L-PBF [19]. The welded L-PBF samples in this research showed better ductility (10%) as compared to those of the L-PBF base metal (3%) and welded cast samples (2.5%).

Recent literature survey documented EBW and laser beam welding of wrought IN718 and some other L-PBF materials. Although TIG welding and brazing were explored to join L-PBF IN718, a study on EBW of L-PBF IN718 is yet to be found. Electron beam welding, which provides excellent penetration depths, weld quality, and mechanical properties, can be utilized to join additively manufactured components for demanding applications. Given its success in joining rolled IN718 [10] and some other L-PBF materials, this research utilizes EBW to join L-PBF IN718. The results are compared with data from rolled IN718 and existing ASTM specifications.

### 3 Materials and methods

Gas atomized IN718 powder was used to manufacture the L-PBF test samples. The average powder size was 50 µm in diameter. The chemical compositions of the powder and rolled IN718 used in this study are summarized in Table 2.

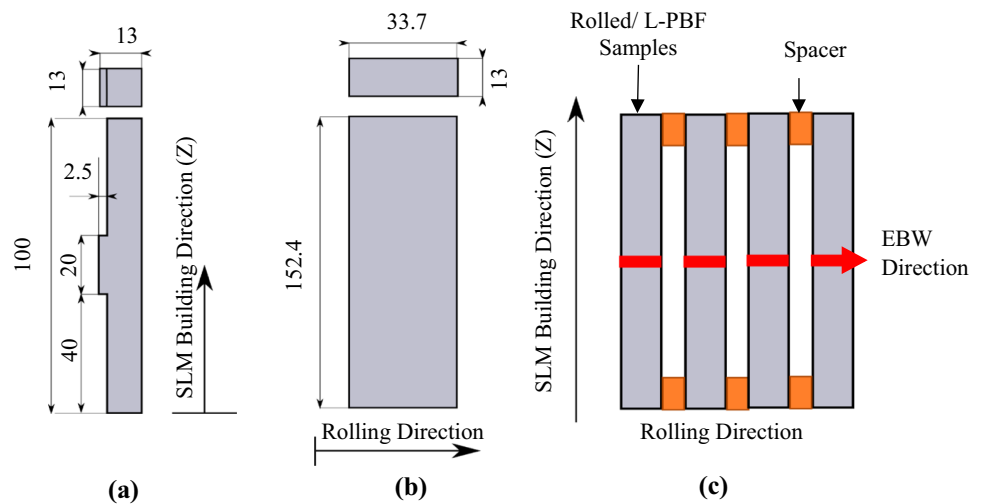
The L-PBF samples were built using the Renishaw AM400 with a maximum capacity of 400 W. The specimens (13 × 13 × 100 mm long) were manufactured using laser power of 275 W, scanning speed of 786 mm/s, hatch distance of 110 µm, and a layer height of 60 µm. The laser beam utilized stripe scanning strategy in an argon atmosphere. Twenty samples were built simultaneously on the same substrate platform such that the building direction matched the loading direction during the subsequent tensile tests. The building scheme is shown in Fig. 1a. The samples were labeled from 11A to 20A and repeating again with 11B to 20B for repeated samples. Hot rolled samples (33.7 × 13 × 152.4 mm long, Fig. 1b) were machined from a commercial wrought plate. The rolled samples were labeled as A11 to A91 and again as A12 to A92 for repeated samples.

All L-PBF samples were arranged next to each other but separated by spacers on the bed of the Sciaky EBW machine as shown in Fig. 1c. Uniform spacers were used for clamping of all samples and to prevent the joining of adjacent samples.

**Table 2** Chemical composition (wt%) of powder [Ref: Luvak Laboratories], rolled IN718 [ Ref: Bolen W (2019) Certified Materials Test Report. West Virginia], and ASM [ Ref: Voort G Vander (1991) Inconel 718 (Alloy 718) and Modified Inconel 718]

	Ni	Cr	Fe	Nb	Mo	Ti	Al	C	Co	Cu	Si	Mg
Powder	51.99	18.58	19.73	5.17	3.02	0.99	0.49	0.024	0.14	0.12	0.073	0.074
Rolled	53.48	18.15	17.88	5.17	3	0.98	0.53	0.03	0.18	0.14	0.09	0.07
ASM	50–55	17–21	~17	4.75–5.5	2.8–3.3	0.65–1.15	0.2–0.8	<0.8	<1.0	<0.3	<0.35	<0.35

**Fig. 1** Schematic arrangement. (a) L-PBF sample. (b) Rolled sample. (c) Typical sample arrangement for EBW. Unit: mm



The EBW system was programmed to produce EBW beads on the samples along the direction perpendicular to the L-PBF building direction. The electron beam was set to focus on the top of each sample without beam oscillation at a constant voltage of 50 kV. It was performed in a contained environment with a vacuum less than 1  $\mu$ Torr. Three variations of each welding speed and beam current were used to give a nine-level design of experiments. Two repeats were welded at each heat input. The electron beam heat inputs for these nine levels varied between 180.4 and 295.3 J/mm as shown in Table 3. The unwelded samples 20A and 20B were used as references. The rolled IN718 samples (A1 to A9) were welded parallel to the rolling direction using the same steps mentioned above. All welded samples were subjected to stress-relieving (SR) at 970 °C for 1 h to remove residual stresses after welding and prevent distortion of samples during subsequent processing.

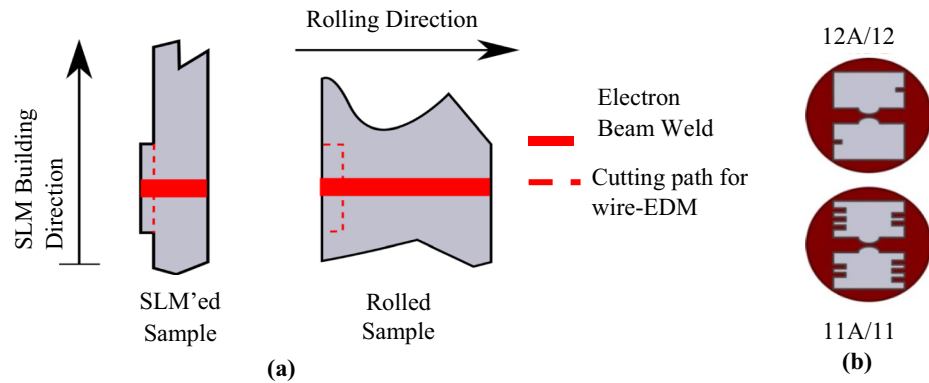
Small L-PBF coupons (2.5  $\times$  13  $\times$  20 mm long) and rolled coupons (6  $\times$  13  $\times$  20 mm long) were removed from the welded samples using wire-type electrical discharge

machining (wire-EDM) process for hardness and microstructure study. Each L-PBF coupon was marked for different EBW parameters and then molded in Bakelite resin with the CitoPress-15 system. Refer to Fig. 2 for schematics of a typical L-PBF hardness test sample. The samples were then ground using the Struers AbriPol-20 semiautomatic grinding machine with grinding wheels Emery-80, Piano MD –80, 220, 500, and 1200 grit in that order. Ground samples were then cleaned ultrasonically in isopropyl alcohol for 30 s. Samples were then polished using a Dremel 3000 hand polisher and diamond pastes of 5–7  $\mu$ m, 1  $\mu$ m, and finally with 0.5  $\mu$ m abrasive size. Samples were ultrasonically cleaned each time before switching to a different sized diamond polishing paste. To reveal the weld features, the coupons were etched by swapping with the Aqua Regia etchant (4 HCl (33%) + 1 HNO<sub>3</sub> (67%)) for 30 s. Tensile samples were wire-EDM from the remnant EBW samples. The thickness of EBW samples was milled to 6 mm thick by removing an equal amount of material from each side before they were wire-EDM to

**Table 3** EBW parameters. Constant 50-kV beam voltage

L-PBF sample label	Rolled sample label	Beam current (mA)	Welding speed (mm/min)	Heat input (J/mm)
11A, 11B	A11, A12	65	660.4	295.3
12A, 12B	A21, A22	60	660.4	272.6
13A, 13B	A31, A32	55	660.4	249.8
14A, 14B	A41, A42	65	787.4	247.6
15A, 15B	A51, A52	60	787.4	228.6
16A, 16B	A61, A62	55	787.4	209.6
17A, 17B	A71, A72	65	914.4	213.2
18A, 18B	A81, A82	60	914.4	196.8
19A, 19B	A91, A92	55	914.4	180.4
20A, 20B	-	-	-	-

**Fig. 2** Schematic for test sample preparation. (a) Wire-EDM of the hardness coupons from welded samples. (b) Marking and molding of L-PBF hardness coupons



the dimensions specified by the ASTM E8 standard for sub-size tensile specimens (Fig. 3).

The weld features, defects, profiles, and dimensions were observed and measured with the Olympus STM6 optical microscope at 0.1  $\mu\text{m}$  resolution. Images captured using the microscope were stitched together using computational image editing tools. The Vega3 Tescan scanning electron microscope (SEM) was used to analyze fractured surfaces. The integrated Oxford X-act Energy Dispersive Spectroscopic (EDS) system was used for elemental analysis. Room temperature tensile tests were conducted using the displacement control method on the MTS-800 universal tensile testing machine with a 100 kN loadcell, at a strain rate of 0.5 mm/min, and at data acquisition frequency of 5 Hz. Toughness was calculated from the area under the stress–strain curve for each sample. Microhardness tests were conducted using the Wilson VH1102 Vickers hardness tester with 300 gf load and 15 s dwell time. Hardness was tested at various locations along and across the weld penetration as shown in Fig. 4. Between the level A (0.3 mm deep from the bead surface) and level B (4.8 mm from the bead surface), microhardness was also measured at four different points along the weld centerline (X direction). Large spacing between indentation was maintained to minimize the work hardening effect that could affect the hardness data.

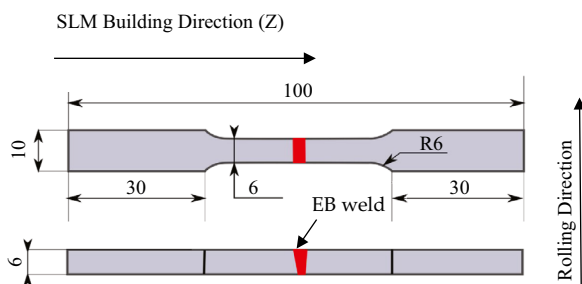


**Fig. 3** Tensile test specimen as per the ASTM E8 standard. Unit: mm

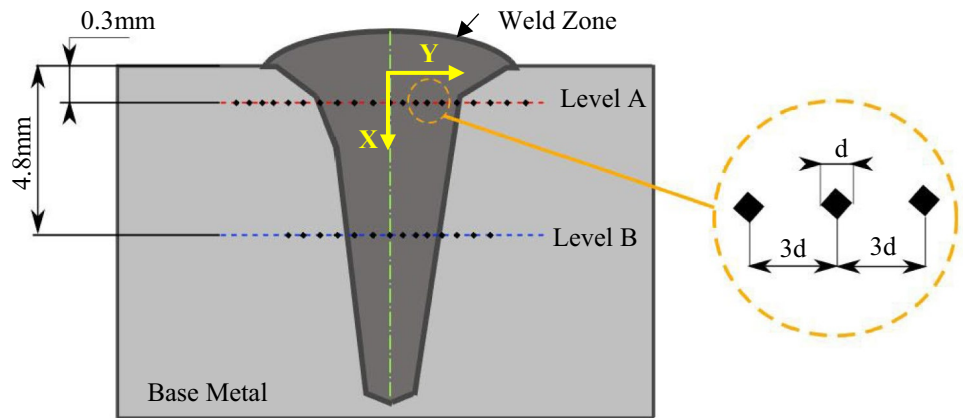
## 4 Results and discussions

### 4.1 Weld profiles and defects

Typical EBW profiles for both the hot rolled and L-PBF samples are shown in Fig. 5. As expected, E-beam can penetrate very deep in metals including IN718 and provide excellent weld penetration. The top of a weld had a wide “nail-head” shape which gradually reduced in width to a slender “nail-point” shape at the bottom. The large weld volume of a nail-head was seen at beam entrance since this volume was subjected to the larger effective beam diameter of the focusing beam, and longer beam exposure time. A higher heat input of the beam allowed larger weld volume and deeper penetration. Full penetration of the 13 mm rolled plate is shown in Fig. 5 when the heat input was 259.3 J/mm, and the welding speed was 660 mm/min (sample A1). Voids (keyholes) were observed at the bottom of the welds due to fast welding speeds as seen in samples A4 (247.6 J/min, 787.4 mm/min) and A7 (213.2 J/mm, 914.4 mm/min) but not in other samples. Similar voids occurred at the welded bottom of L-PBF samples (Fig. 6a), and additional voids were found near the HAZs of the weld head (Fig. 6b). No similar voids were found at the nail-head of the rolled samples welded at the same E-beam parameters. Thus, it was postulated that the voids at the nail-head originated from pores/defects in the L-PBF and worsened due to solidification shrinkage of the molten metal in the weld. This hypothesis was further supported by observations in the twin samples where no void was seen. Both rolled samples A8 (and its twin) and L-PBF sample 18A (and its twin) showed no void in the weld joined at low 196.8 J/mm heat input.

Figures 7 and 8 respectively show the linear dependency of weld penetration depth on heat input and weld area (excluding void area) against the beam current. A slow beam speed allowed more interaction time between the beam and the material, therefore, formed a larger molten volume and weld area. Deeper penetration was found for rolled samples as compared to L-PBF samples at the same heat inputs.

**Fig. 4** Microhardness testing across a typical weld



Since the beam accelerated voltage was kept constant at 50 kV, the weld area also increased with higher heat input.

## 4.2 Tensile properties

When fabricating the tensile specimens, any pores and defects on the top and bottom of a weld were machined away on both sides to reduce all sample thicknesses from 13 to 6 mm per the ASTM E8 standard. Thus, the welded specimens in this study simulated the ideal scenario when separated workpieces were perfectly aligned and then welded for through-thickness penetration. All the L-PBF welded samples were fractured at the weld except for the sample 16A. Both the as-printed samples (20A-B) were broken away from the center of the specimens. Figure 9 plots typical stress–strain curves of the welded L-PBF twin samples (19A-B); similar plots for the rolled IN718 twin samples (A91-2) are superimposed for comparison.

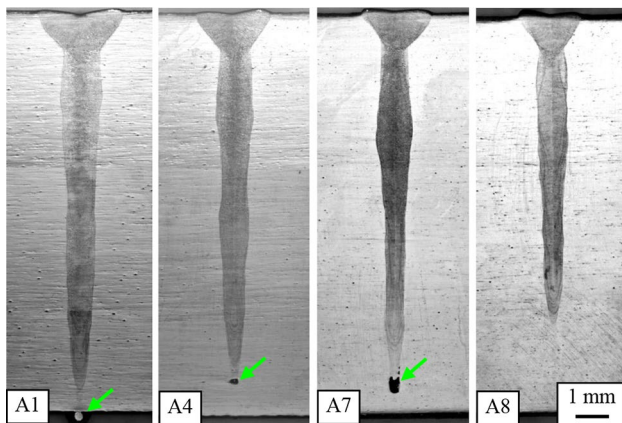


**Fig. 5** Typical nail shaped welds in rolled samples: (A1) at 295.3 J/mm with through-thickness penetration, (A4) at 247.6 J/mm and (A7) at 213.2 J/mm with the voids at weld bottom (at arrows), and (A8) at 196.8 J/mm. Similar profiles were seen for all L-PBF samples

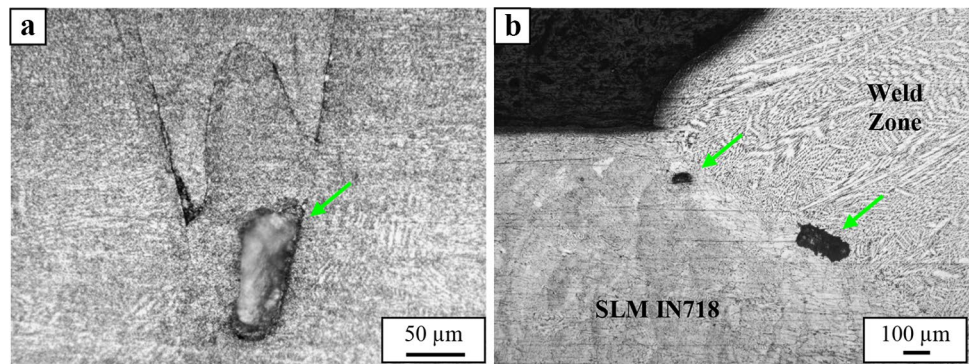
At the same EB welding parameters, it was found that:

- The stress–strain curves of twin samples repeated very well.
- The yield and tensile strengths of L-PBF samples were higher than those from the rolled samples
- The ductility and toughness (area under stress–strain curve) of typical L-PBF material, however, were less than those of the rolled material.

Table 4 summarizes and compares tensile properties for each twin pair of L-PBF and rolled samples. Recall that the twin samples 20 A-B were printed by L-PBF but not subjected to EBW. Figure 10a–c compare the mechanical properties of EB-welded samples of rolled and L-PBF samples. The data show that:

- All L-PBF samples exceeded the minimum yield strength of 600 MPa, specified in the ASTM F3055-14a standard for additively manufactured IN718. The yield strengths of L-PBF samples also exceeded those of the rolled samples (Fig. 10a).
- When comparing the tensile strength, at least one replicate of each sample exceeded 920 MPa, specified in the ASTM standard, except for sample 18A-B (196.8 J/mm). Again, all the tensile strength of L-PBF samples exceeded those of their rolled counterparts (Fig. 10b).
- All the EBW'ed L-PBF samples had low ductility; therefore, they neither met the ASTM standard nor could compare to the ductility of the rolled samples (Fig. 10c). The as-printed samples (20A-B) with 27.7–28.0% elongation was marginally met the ASTM standard requirements for elongation (27%) but were inferior to that of the rolled samples. The brittleness of L-PBF samples can be explained by the resulted microstructures that are presented in the fractography section.

**Fig. 6** Voids at arrows. (a) At weld bottom of L-PBF sample 13A at 249.8 J/mm. (b) At nail-head of L-PBF sample 17A at 213.2 J/mm. These defects, however, were absent in the duplicated specimens



- Using the electron beam parameters selected for this study, the mechanical properties of EBW samples were inferior to those of the as-printed samples (sample 20 A/B, Table 4). Although both tensile strength and yield strength met the ASTM specifications, the ductility of all welded samples did not due to EBW-induced defects. Perhaps appropriate post processing techniques must be used in conjunction with EBW to improve the ductility of welded specimens.

Recall that the electron beam voltage was kept the same at 50 kV while varying both beam current and beam speed in this study. Yield strength, tensile strength, and elongation of welded samples are plotted against the beam speed and beam current in Figs. 11, 12, and 13 respectively. Although there is no definite dependence of mechanical properties on either beam current and beam speed for the hot rolled samples, the mechanical properties of L-PBF were lower for samples with high beam scanning speed (914.4 mm/min) and high currents (60–65 mA). Both conditions would provide (i) a higher melting temperature of a melt pool due to higher current and power density, (ii) faster cooling rate due to fast beam speed from a higher temperature; such combination would promote the formation of Laves, brittle carbide/oxide

particles and trapped pores that collectively downgrade the mechanical properties. Referring to Table 3 and Eq. (2), these combinations give the heat input values of 196.8 and 213.2 J/mm, respectively; the average heat input for these two values is 205 J/mm. The inferior mechanical properties, i.e., low strength and low ductility of samples when EBW about 205 J/mm are seen in Fig. 10a–c.

### 4.3 Microhardness

Referring to Fig. 4, the co-ordinate system XY has the origin located at the top of a weld zone, and the X-axis is along the weld center. Microhardness data across a typical weld zone (L-PBF sample 19A) is shown in Fig. 14). The vertical blue dashed lines indicate the weld-zone in the larger nail-head region while the vertical orange dotted line indicates the narrower weld-zone towards the weld-bottom. Table 5 compares the hardness of the weld-zone and the surrounding parent material of both samples.

The following observations are deduced from Table 5 and Fig. 14:

- The material in the weld-zone is softer than that of parent material for both L-PBF and rolled samples. The rapid

**Fig. 7** Effect of beam heat input on weld penetration

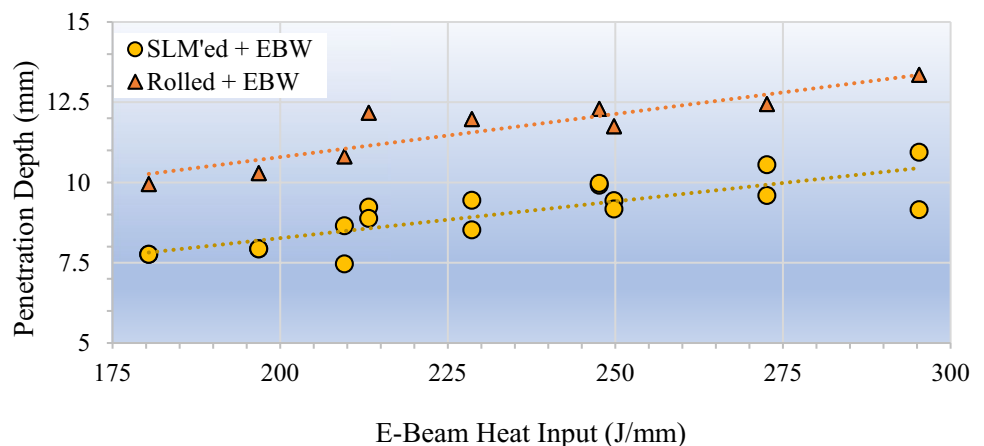
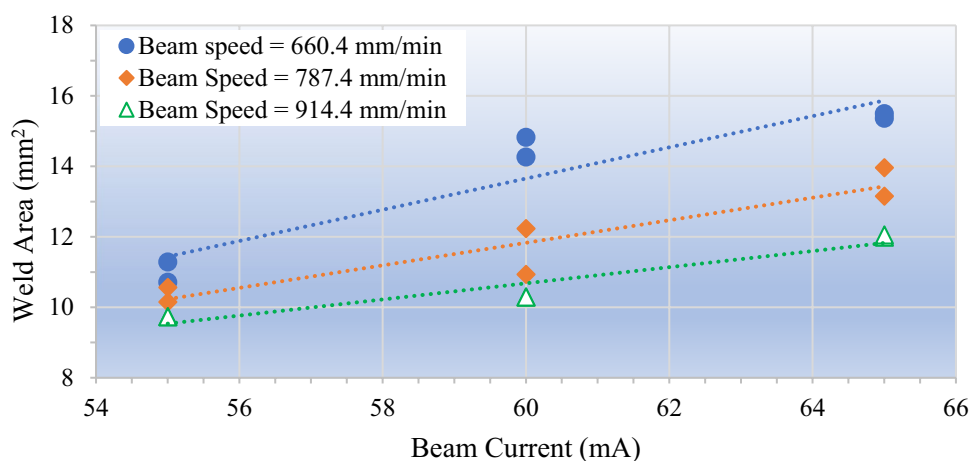




**Fig. 8** Effects of beam parameters on the weld area of L-PBF samples



heating and cooling of the weld zone formed finer columnar grains in the weld (Figs. 5 and 6b) but also generated the inter-crystallite  $\delta$  phases at the grain boundaries and reduced the overall hardness [9]. In the rolled sample, melting in the weld zone effectively wiped off the preferred grain orientation and grain boundary hardening effect after rolling, therefore resulted in lower hardness values.

- The material at the nail-head (beam entrance zone) is softer than that of a weld zone below. Due to the slight taper of the focused electron beam, the larger nail-head volume was subjected to a larger beam area and longer heating time; the resulting lower beam power density at the longer heating time promoted grain growth and softened the material.
- The weld area at the nail head is larger on the L-PBF material than that on the rolled material when EBW at the same parameters. Perhaps such results were due to the differences in thermal conductivity, internal defect, and viscosity of the two materials.
- The L-PBF material is harder than the rolled material. The rapid heating and cooling of IN718 formed the Nb-rich Laves and metallic carbide particles in the micro-

structure. Although these Laves and carbide particles are larger than typical precipitates, they would impede the motion of dislocations, thus increase the material hardness. Evidence of Laves and carbide particle formation will be seen in the next section where the study of fracture surfaces of tensile samples is presented.

#### 4.4 Fractography

Analysis of fractured surfaces reveals useful information that explains the tensile properties of tested samples. This section presents fractured surfaces of selected L-PBF and rolled samples and compares the fracture surfaces inside and outside of corresponding welds. Figure 15 shows the SEM images of the fractured surface of rolled EBW sample A81 (196.8 J/mm) that broke outside the weld. Fracturing outside of a weld zone indicated the success of the EBW samples at one of the optimal welding parameters. It was postulated that the normal fractured surface started in the central zone and propagated outward; when the fractured surface area exceeded a critical size, the rapid final fractures occurred near the outer surfaces in shear mode as indicated with about 45° slopes (Fig. 15a).

**Fig. 9** Typical stress–strain curves for rolled and L-PBF specimens welded at 180.4 J/mm. A slight strain offset of 0.01 for samples 19AB and stress offset of 20 MPa are plotted for better visualization

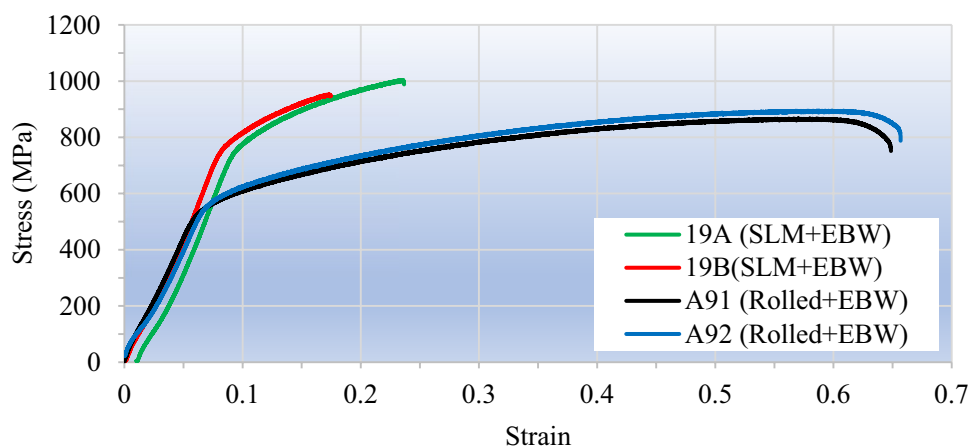


**Table 4** Mechanical properties of EBW'ed L-PBF IN718 samples

Sample label	EBW heat input (J/mm)	YS (MPa)	UTS (MPa)	Young's modulus (GPa)	Ductility (%)	Toughness (J/mm <sup>3</sup> × 10 <sup>-3</sup> )
11 A/B	295.3	720, 722	937, 998	10.9, 10.5	16.9, 22.5	102, 155
12 A/B	272.6	715, 724	925, 987	11.0, 10.5	17.0, 20.6	98, 143
13 A/B	249.8	722, 703	951, 1004	10.8, 10.4	19.1, 22.3	117, 161
14 A/B	247.6	714, 724	899, 967	10.9, 10.7	15.1, 18.2	85, 102
15 A/B	228.6	737, 706	976, 932	10.9, 10.6	19.5, 16.8	125, 103
16 A/B	209.6	724, 709	889, 931	10.7, 11.6	15.8, 16.4	87, 102
17 A/B	213.2	719, 712	927, 899	10.9, 10.8	18.8, 13.4	125, 75
18 A/B	196.8	702, 708	891, 888	10.7, 11.2	16.5, 14.0	88, 77
19 A/B	180.4	735, 710	1004, 953	10.9, 11.1	22.7, 17.5	159, 110
20 A/B	-	741, 745	1045, 1024	10.8, 10.9	28.1, 27.7	210, 198

In the central region of the sample, isolated dark and brittle particles were seen throughout the surface (Fig. 15b). Recall that the chemical composition of IN718 materials in this study (Table 2) was within the ASM specifications. The EDS

spectrums (Fig. 16) of a zone outside of such particle confirmed the correct chemical composition of IN718; however, analysis of points on the particle showed excessive niobium (Nb) and titanium (Ti) contents with a reduced amount of

**Fig. 10** Effect of E-beam heat input on (a) yield strength, (b) tensile strength, and (c) elongation of welded samples. The thresholds for minimum acceptance values from ASTM specification are included

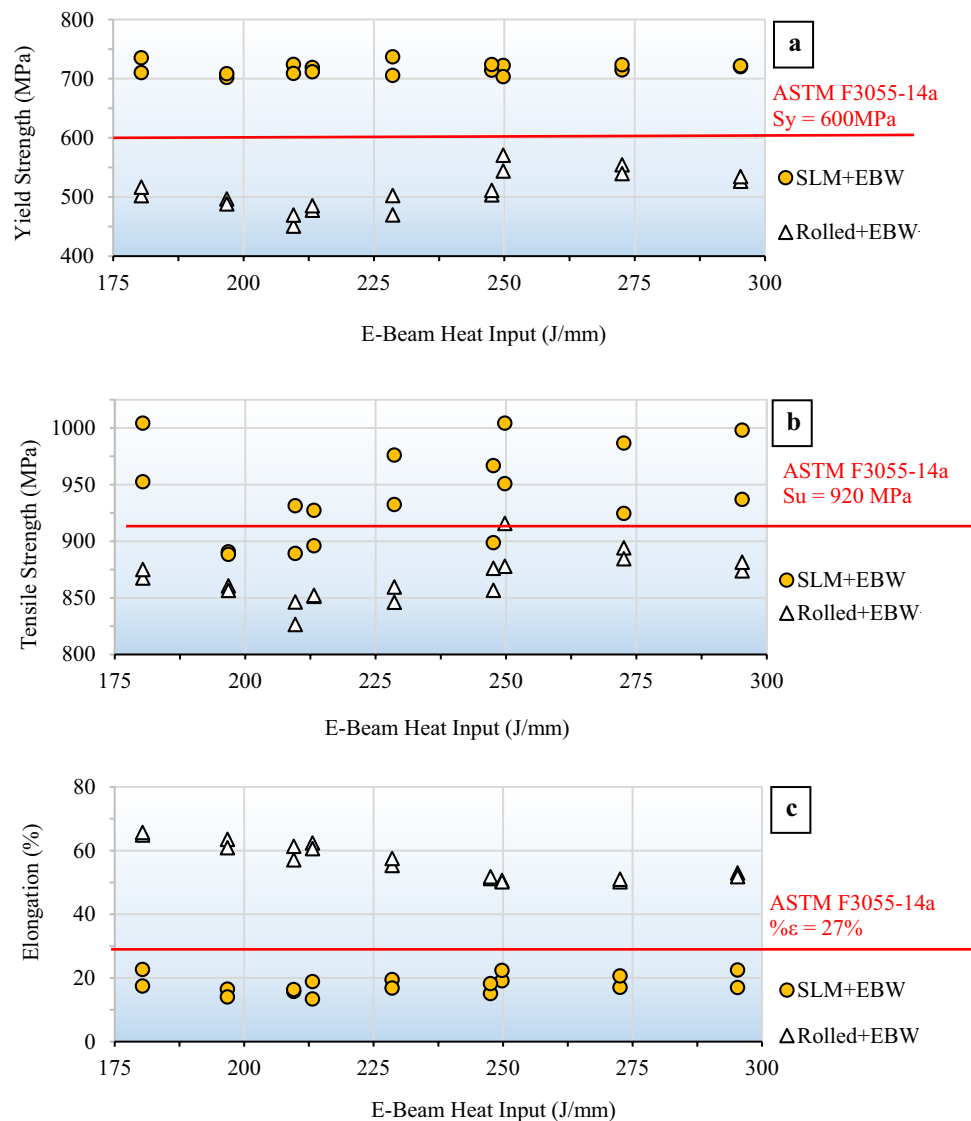
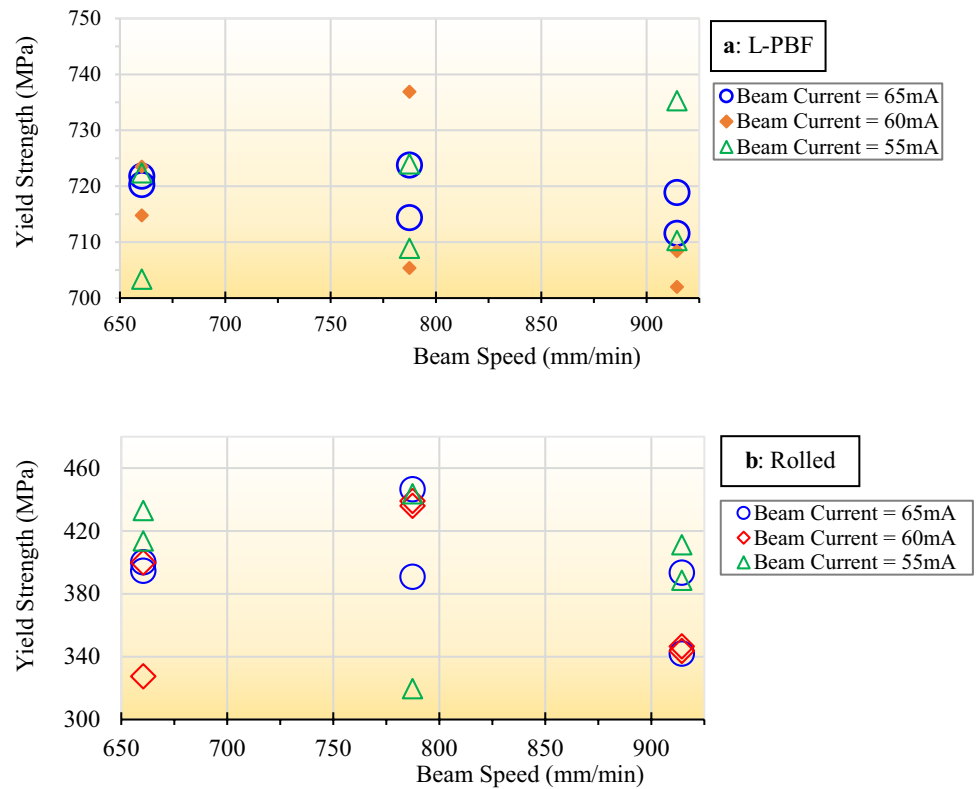


**Fig. 11** Effect of beam parameters on yield strength of (a) L-PBF and (b) rolled samples



nickel (Ni) and chromium (Cr). Such (Nb, Ti) intermetallic compounds degraded the material. Although the number of these brittle particles, and its volumetric density, were

relatively small to significantly affect the tensile properties, they were the crack nucleation sites that certainly degraded the fatigue and creep property of such a sample.

**Fig. 12** Effect beam parameters on tensile strength of (a) L-PBF and (b) rolled samples

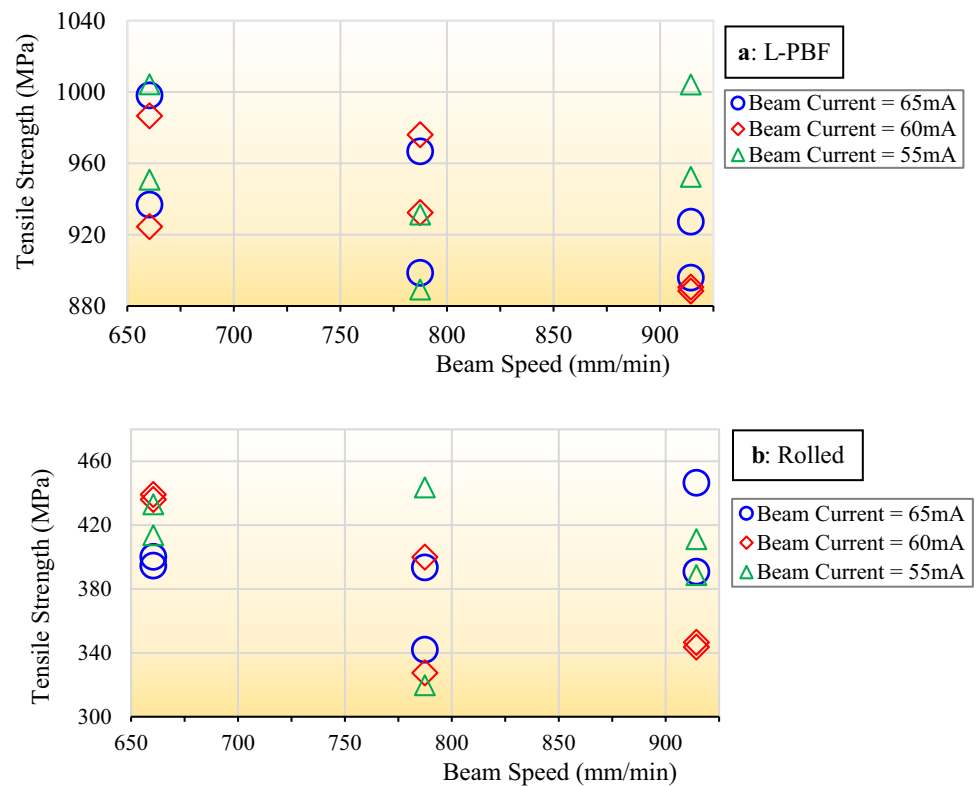


**Fig. 13** Effect of beam parameters on elongation of (a) L-PBF and (b) rolled samples

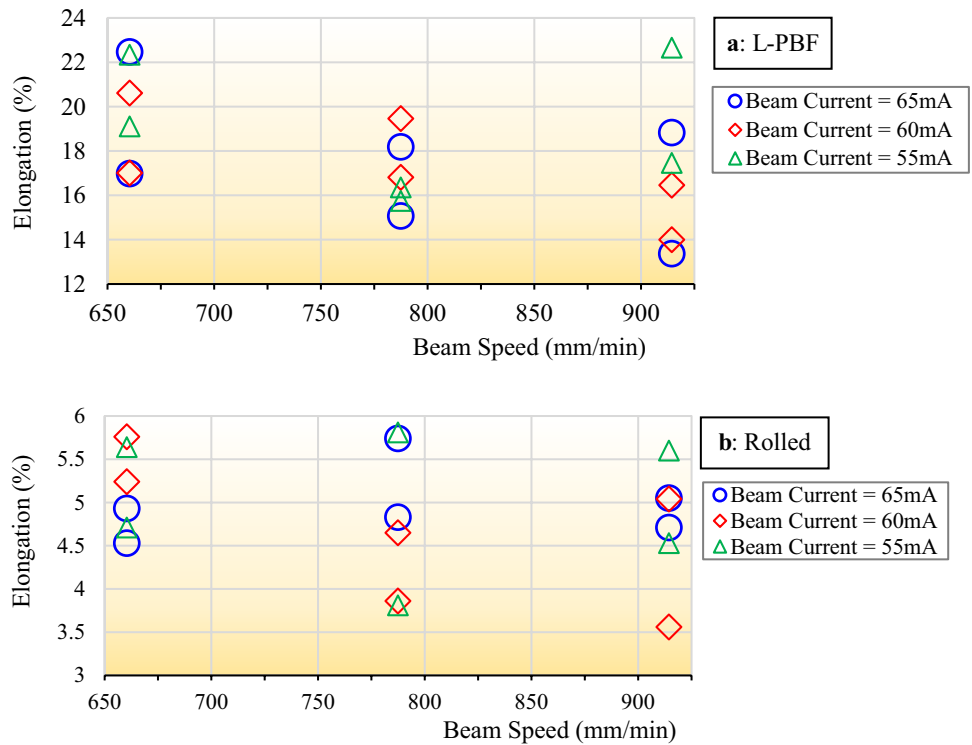
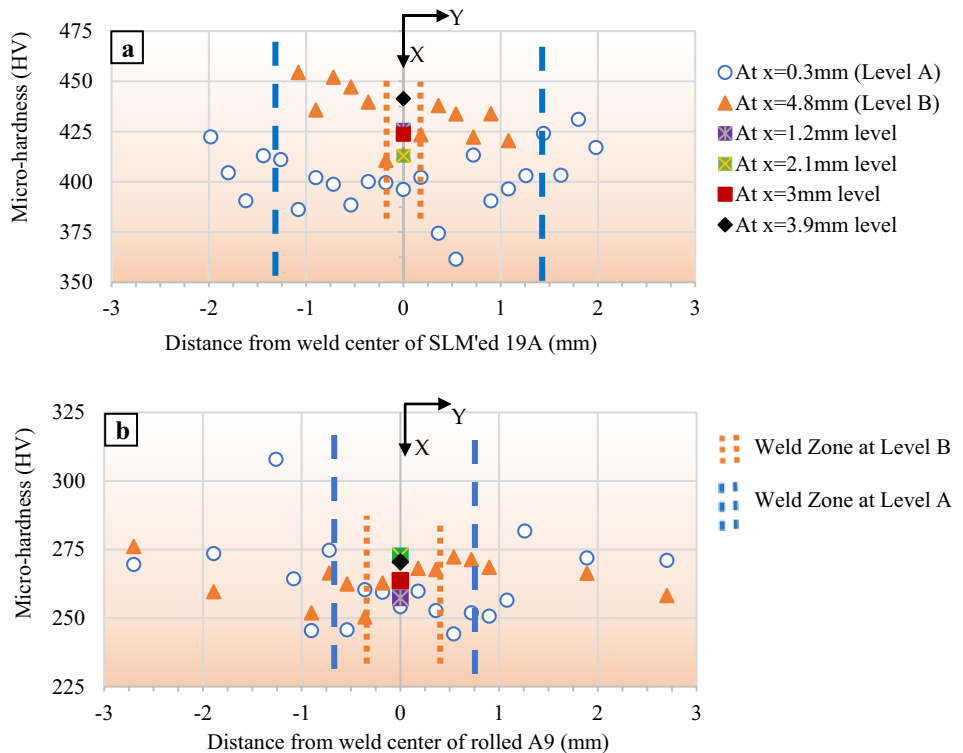


Figure 17 shows the fractured surface inside the weld zone of the rolled sample A21 (272.6 J/mm). Similar fracture mechanism is proposed: normal fractured surface started in the central zone and propagated outward, followed by the final and rapid shear fractures near the outer surfaces

(Fig. 17a). Very fine and ductile grains were seen due to the relatively fast cooling of the small weld surrounded with a larger volume of the parent material. Isolated (Nb, Ti) brittle particles were visible inside the ductile matrix as confirmed with EDS analysis (Fig. 17b).

**Fig. 14** Typical microhardness test results. (a) L-PBF sample 19A. (b) Rolled sample A9 welded at the same heat input of 180.4 J/mm



**Table 5** Vickers microhardness (HV) of samples with the same heat input 180.4 J/mm

	Parent material		Weld-zone	
	L-PBF	Rolled	L-PBF	Rolled
Weld top ( $x=0.3$ mm)	$413.2 \pm 12.3$	$269.2 \pm 16.7$	$394.9 \pm 12.9$	$255.8 \pm 8.6$
Weld center ( $x=4.8$ mm)	$437.7 \pm 10.7$	$265.3 \pm 6.94$	$415.9 \pm 5.4$	$264.3 \pm 7.6$

Fractured surface of the as-printed L-PBF sample 20A revealed volumetric defects due to laser interaction with the IN718 powder. The fractured surface in Fig. 18 shows:

- Partially melted IN718 powder particles and unfilled zones (Fig. 18a). These stress-raiser sites would degrade the mechanical properties of L-PBF materials.
- Large chunks of brittle phases with irregular shapes were plentiful on the surface (Fig. 18b). EDS analysis that showed carbon, titanium and aluminum suggested such brittle phases were metallic carbides.

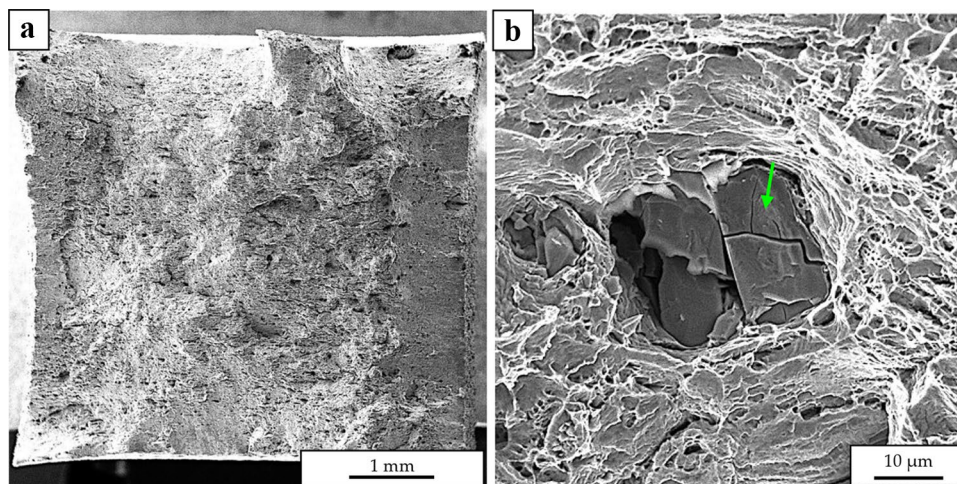
Figure 19 shows the fractured surface of the L-PBF sample 17A that broke inside the weld. The very-ductile matrix was evidenced with dimple fracture surface and fine grains. Distinct brittle features of a circular particle and white regions (labeled “1” and “2”) were seen. The EDS analysis at different locations (Fig. 19) showed the weight percentage of Nb in the ductile matrix was normal for Nb (4.7%, that is nearly within the 4.74–5.5% from ASM specification) and Al (0.7%, that is within the 0.2–0.8% from ASM specification). However, the levels for Nb (6.1–9.9%) and Al (1.0–3.2%) of the circular brittle particle were much higher than the maximum chemical levels of the surrounding IN718 matrix. This confirmed that those brittle particles were the Laves phase and consistent with published literature. The regions at points 1 and 2 (i) contained high oxygen concentration (2.6–4.0%), Nb (9–9.9%), and lower Ni/Cr/Fe contents; (ii) did not bond to the IN718 matrix; and (iii) appeared bright white against the darker surrounding matrix in secondary

electron SEM; these oxidized regions were defects where cracks would originate and contributed to the low ductility of L-PBF samples.

Other defects were found of fractured surface in the fusion zone of sample 17B (heat input 213 J/mm). Fractured of gas-filled spherical pores (Fig. 20) that served as sites with high stress concentration; an un-melted spherical particle that was delaminated from the ductile matrix (Fig. 20). Although the shape and size of this particle were similar to the virgin IN718 powder, it must be a different material since it was not melted and had no bond to the surrounding IN718 matrix. At a different location on this sample, a remnant of a brittle spherical particle is shown in Fig. 21a. The EDS analysis (Fig. 21b) of this particle showed the unusual chemical compositions of oxygen (49–51.4%), aluminum (35.6–37.7%), and titanium (7.3–9.6%) as compared to those from the surrounding materials (0% oxygen, 0–0.6 aluminum, and 0–1% titanium). It was assumed that the spherical particle in Fig. 21 was similar to that in Fig. 20 when comparing the shape, relative size, and similar delamination from the matrix. Since aluminum oxide ( $\text{Al}_2\text{O}_3$ ) has stoichiometric composition of 52.9% Al and 47.1% O, the spherical particle in Fig. 21 with 35.6–37.7% Al and 49–51.4% O are not aluminum oxide but an (Al, Ti, O) compound. However, Popovich et al. [20] studied different heat treatments of IN718 and reported the finding of brittle aluminum oxides.

When studying the fractured surface of sample 16A1, addition defects were found that caused it to fracture

**Fig. 15** Fractured surface located outside of the weld zone of sample A81 (rolled + EBW at 196.8 J/mm). (a) Overall view. (b) Typical shattered brittle particles (at arrows) near the center of sample. Notice the distortion in (a) of the square sample due to lens effect of SEM system



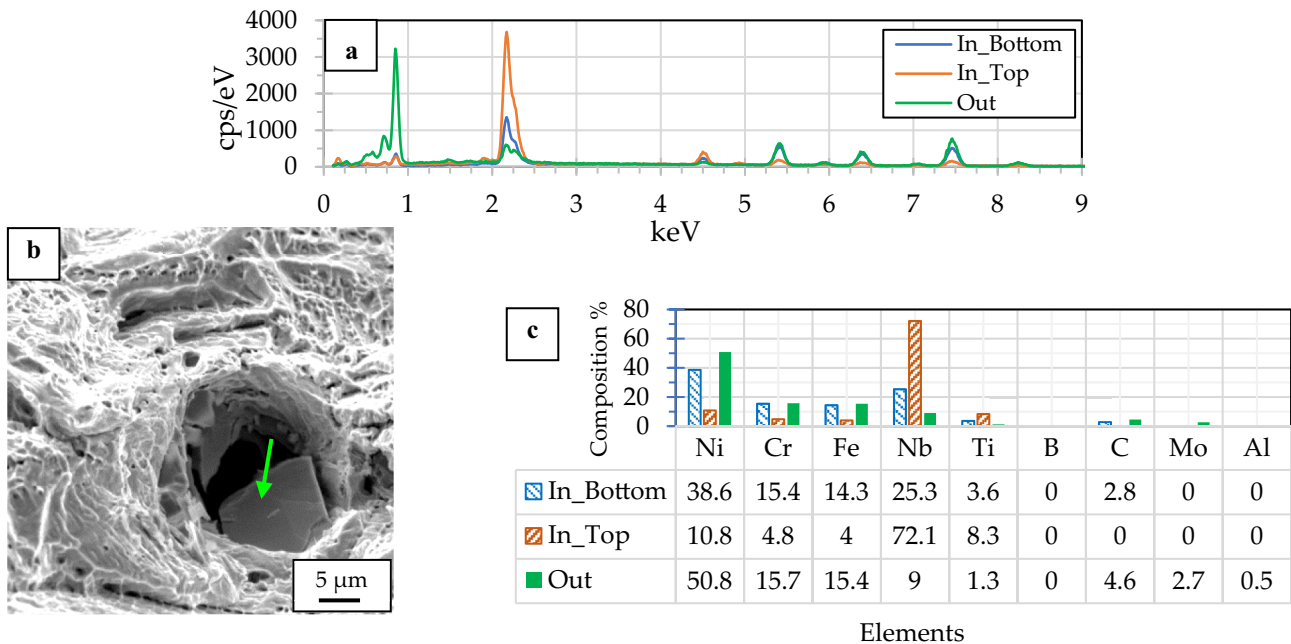


**Fig. 16** (a) A typical brittle particle in specimen A81 (rolled+EBW at 196.8 J/mm). (b) EDX spectrum of points at the top, bottom, and outside of the particle. (c) Resulting chemical analysis

outside of its weld zone. Large zones of delaminated layers were seen (Fig. 22a) perhaps due to inadequate heat input of 209.6 J/mm. Remnants of spherical pores (Fig. 20a) and scattered of brittle Laves or carbide phases were also observed (Fig. 22b).

Both the L-PBF and EBW processes melt and solidify IN718. Local defects can be formed due to different cooling rates. Solidification of IN718 underwent three stages [21]:

- Firstly, the liquid phase transformed into the secondary  $\gamma$  phase and led to precipitation of solute particles such as Nb, C, Ti, in the inter-dendritic region.

- Secondly, the segregation of the particles led to the formation of intermetallic carbides. All or most percentages of carbon in the alloy were consumed in this process; the higher the percentage of carbon in the base alloy matrix, then the higher was the tendency of the carbide formation.
- Thirdly, further enrichment of the solute led to the formation of the Laves phases or carbide phases before the ending of the solidification process.

The formation of the Laves phase was directly proportional to the presence of segregated niobium. The Nb

**Fig. 17** Fractured surface located inside of the weld zone of sample A21 (rolled+EBW at 272.6 J/mm). (a) Overall view. (b) Typical shattered brittle particles (at arrow) near the sample central zone. Notice the ductile failure of surround matrix

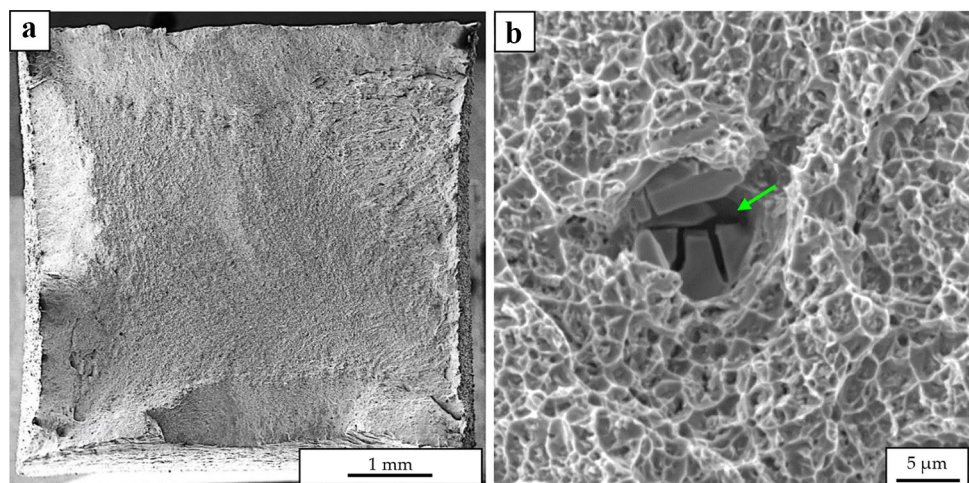
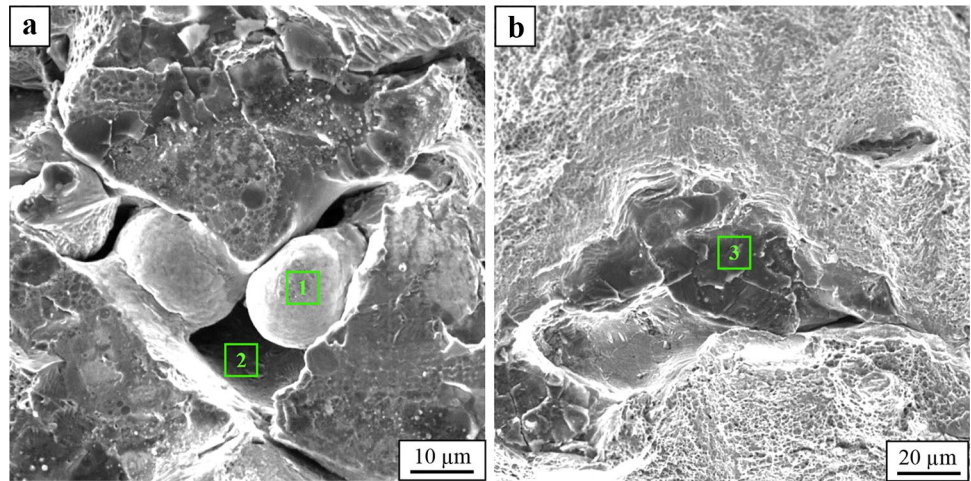


**Fig. 18** Defects on fractured surface of sample 20A (as printed) include (a) partially melted spherical powders (label 1), unfilled zone (label 2), and (b) a brittle particle (label 3) in the ductile matrix



segregation depended mainly on the cooling rate of the molten alloy. A higher cooling rate would lower the segregation of niobium [21]. Thus, favorable material characteristics can be observed at high cooling rates during L-PBF or EBW. Niobium presence in the alloy solution was shared by various secondary phases ( $\delta$ ,  $\gamma$ ,  $\gamma'$ , and  $\gamma''$ ) during solidification. Thus, the higher percentage of any of these phases led to a more reduction in the percentage of the others. In the case of weld-zone, percentage of the strengthening phase  $\gamma'$  and  $\gamma''$  was reduced due to high consumption of Nb by the  $\delta$  and  $\gamma$  phases [9, 21]. Further, the formation of Laves and  $\delta$  phase in the grain boundaries provide favorable sites for nucleation of voids and fissures. This led to poor mechanical properties and hardness of the welds as compared to that of the base metal. Further, the presence of un-melted particles, voids, pores, and oxides

that prevent adhesion between adjacent layers contribute to brittleness in L-PBF parts.

In summary, the low ductility of welded L-PBF IN718, measured by tensile testing in this study, was due to:

- Un-melted or partially melted powder particles and lack of fusion in L-PBF samples (Fig. 18).
- Inevitable gas-filled spherical pores (Fig. 20a).
- Delamination of oxide regions (Fig. 19a), or metallic oxide spherical particles and the surrounding matrix (Fig. 20b).
- Brittle Laves and other carbide phases (Fig. 18b).
- Unfavorable size and distribution of precipitates.

The L-PBF process-induced thermal gradients between adjacent layers thereby fusing them and leading to a

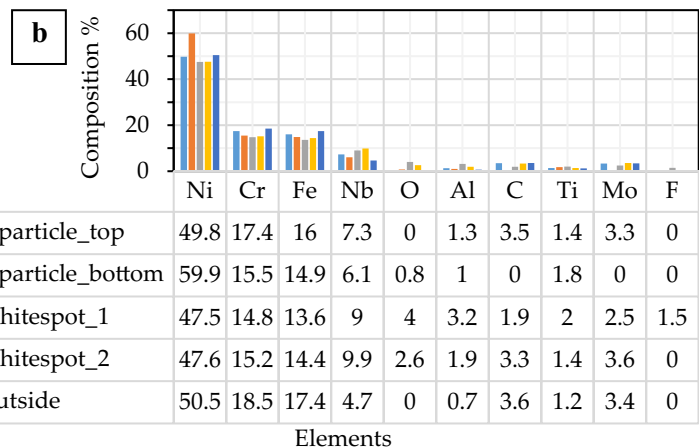
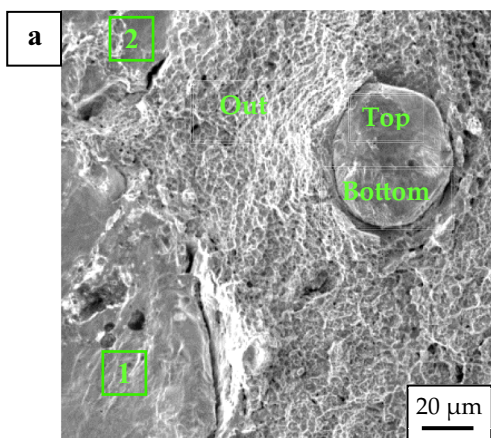
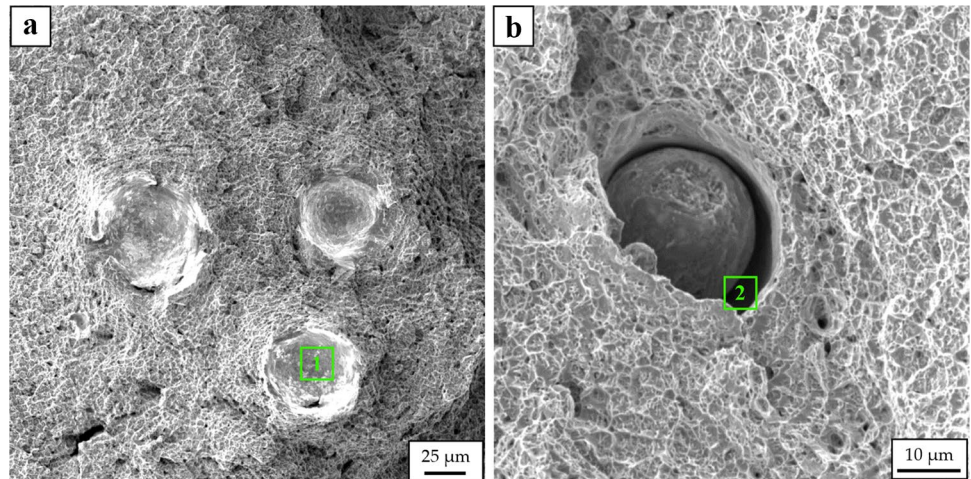


**Fig. 19** The fractured surface at a location inside the weld of sample 17A (L-PBF+EBW at 213 J/mm) showing (a) brittle circular particles and white region labeled “1” and “2” and (b) EDS analysis at different locations

**Fig. 20** The fractured surface inside the weld of sample 17B (L-PBF+EBW at 213 J/mm) showing (a) remnant of spherical pores (label 1) and (b) an un-melted spherical powder in the ductile matrix. Notice the delaminated layer (label 2) between the powder and surrounding ductile matrix



formation of homogenous metal in an ideal case. Uneven layer thickness, fluctuation of laser power, powder contamination can form gaps between the adjacent layers (Fig. 22a). This led to inadequate heat distribution and left some powder particles partially melted (Fig. 18a). Spherical pores were also observed throughout the samples (Figs. 20a, and 22a). Porosity can be formed due to various mechanisms [22]:

- Presence of voids between the partially melted powder particles,
- The collapse of molten pool depression due to high scanning speeds,
- Denudation of un-melted particles surrounding the laser beam path,

- Impartial melting and fast cooling at the end of the laser path on a layer, and
- Original voids in atomized metallic powder.

Towards the end of the scanning path, the beam quickly changed direction, or turned off, leading to the reduction of temperature at the molten surface at the end of the path, thus (i) increased the molten material viscosity, (ii) hindered the flow of molten metal, and (iii) led to a formation of the void at the center of the melt pool [10]. This explained the presence of voids towards the edge of the L-PBF samples. The same mechanism also explained the presence of voids at the HAZ or boundary of the EBW fusion zones. Keyhole defects at the bottom of the welds with high heat inputs also occurred due to the same mechanism.

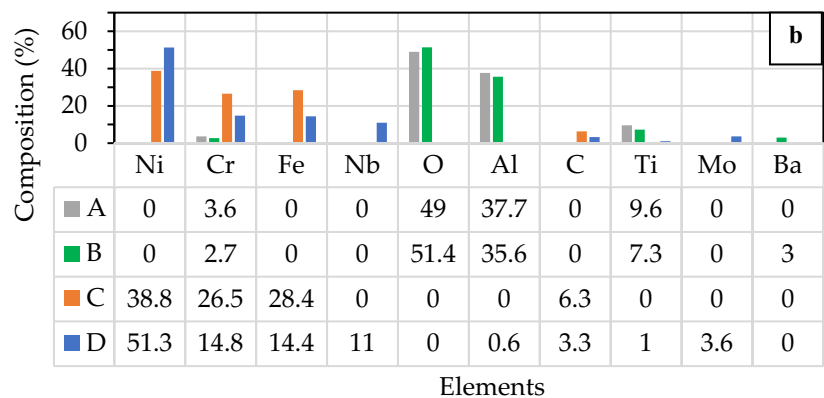
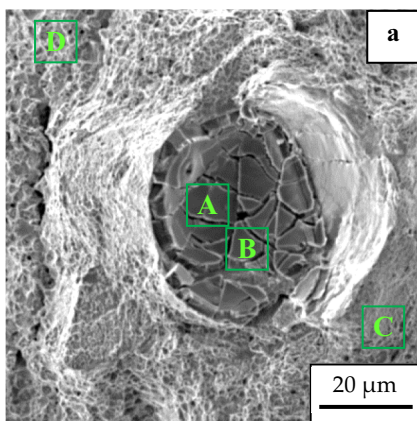
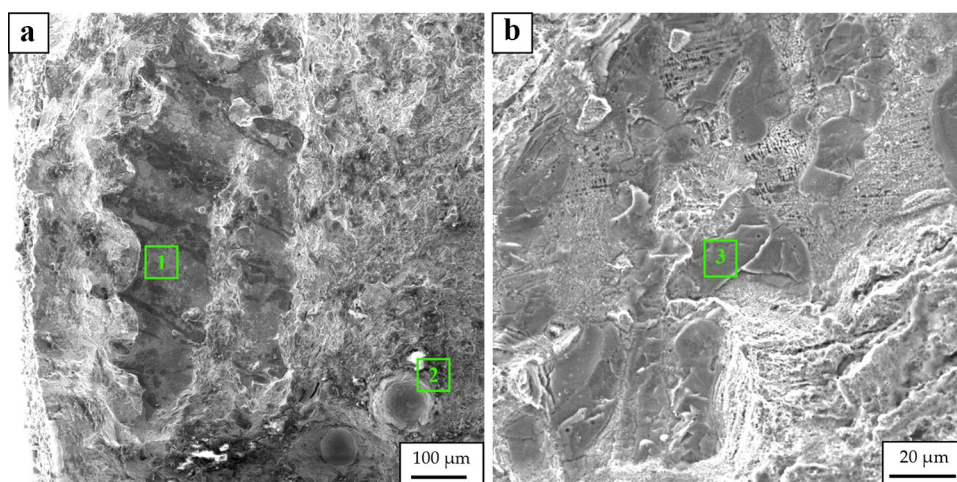


**Fig. 21** The fractured surface at a location inside the weld of sample 17B (L-PBF+EBW at 213 J/mm) with (a) fractured spherical particle and (b) EDS analysis at different locations indicating presence of Al and Ti oxides



**Fig. 22** The fractured surface outside of the weld zone of sample 16A1 (L-PBF + EBW at 209.6 J/mm) showing (a) delamination of layers (label 1) and spherical pores (label 2), and (b) a brittle Laves phase (label 3)



## 5 Conclusions and recommendations

Feasibility of electron beam joining for hot-rolled and laser powder bed fused Inconel 718 (IN718) samples were performed. This study showed:

1. Excellent penetration depths of EBW'ed IN718 can be achieved. Through-thickness penetration of 13 mm plates was obtained with a direct electron beam path without oscillation at 295.3 J/mm heat input. The penetration depth was proportional to the beam heat input.
2. Weld zone was found to be slightly softer as compared to the base metal hardness. This was probably due to formation of tiny pores, larger grains, and  $\delta$  phases in the weld in lieu of the strengthening  $\gamma'$  and  $\gamma''$  precipitates. Vickers hardness at the top of the weld (beam entrance) was also lower than that near the welded bottom due to a faster cooling rate inside the sample.
3. The welded L-PBF material exhibited higher tensile / yield strengths than the rolled materials; however, the ductility of welded L-PBF material was inferior to that of rolled material. The welded L-PBF material met the strength requirement from ASTM F3044-14a specifications but failed the requirement for ductility.
4. High beam scanning speed at high beam power promoted the formation of Laves, brittle carbide/oxide particles and trapped pores. The inferior mechanical properties of L-PBF samples at these conditions were experimentally found and verified with fractographic study.

Further enhancement to the quality of welded L-PBF IN718 can be achieved by:

- (a) Optimizing of the L-PBF process parameters to completely melt the powder and satisfactorily join adjacent layers.

- (b) Utilizing the oscillating electron beam in welding for higher quality welds.
- (c) Applying suitable post-processing methods such as hot isostatic pressing to as-printed material to eliminate most of the interior voids, and homogenizing to dissolve Nb-rich Laves particles. Suitable solution heat-treating and aging can also be implemented to achieve the balance between strength and ductility of welded materials.

**Acknowledgements** The authors thank Mr. Rodney Inmon (Materials Testing Lab, Department of Aerospace Engineering) and Mr. Tom Stephens (Microscopy and Imaging Center) for their assistance. We thank KGSBO for providing in-kind material and equipment support.

**Author contribution** All authors contributed equally to this study.

## Declarations

**Ethics approval** Not applicable.

**Consent to participate** Not applicable.

**Consent for publication** Not applicable.

**Conflict of interest** The authors declare no competing interests.

## References

1. Akca E, Gürsel A (2015) A review on superalloys and IN718 nickel-based INCONEL superalloy. *Period Eng Nat Sci* 3. <https://doi.org/10.21533/pen.v3i1.43>
2. Slama C, Abdellaoui M (2000) Structural characterization of the aged Inconel 718. *J Alloys Compd* 306:277–284. [https://doi.org/10.1016/S0925-8388\(00\)00789-1](https://doi.org/10.1016/S0925-8388(00)00789-1)
3. Norrish J (2006) High-energy density processes. In: Norrish J (ed) *Advanced welding processes*. Elsevier, pp 136–164
4. Hong JK, Park JH, Park NK, Eom IS, Kim MB, Kang CY (2008) Microstructures and mechanical properties of Inconel 718 welds

- by CO<sub>2</sub> laser welding. *J Mater Process Technol* 201:515–520. <https://doi.org/10.1016/j.jmatprotec.2007.11.224>
5. Huang CA, Wang TH, Lee CH, Han WC (2005) A study of the heat-affected zone (HAZ) of an Inconel 718 sheet welded with electron-beam welding (EBW). *Mater Sci Eng A* 398:275–281. <https://doi.org/10.1016/j.msea.2005.03.029>
  6. Madhusudhana Reddy G, Srinivasa Murthy CV, Srinivasa Rao K, Prasad Rao K (2009) Improvement of mechanical properties of Inconel 718 electron beam welds-influence of welding techniques and postweld heat treatment. *Int J Adv Manuf Technol* 43:671–680. <https://doi.org/10.1007/s00170-008-1751-7>
  7. Agilan M, Venkateswaran T, Sivakumar D, Pant B (2014) Effect of heat input on microstructure and mechanical properties of inconel-718 EB welds. *Procedia Mater Sci* 5:656–662. <https://doi.org/10.1016/j.mspro.2014.07.312>
  8. Mei Y, Liu Y, Liu C, Li C, Yu L, Guo Q, Li H (2016) Effect of base metal and welding speed on fusion zone microstructure and HAZ hot-cracking of electron-beam welded Inconel 718. *Mater Des* 89:964–977. <https://doi.org/10.1016/j.matdes.2015.10.082>
  9. Gao P, Zhang KF, Zhang BG, Jiang SS, Zhang BW (2011) Microstructures and high temperature mechanical properties of electron beam welded Inconel 718 superalloy thick plate. *Trans Nonferrous Met Soc China English Ed* 21:s315–s322. [https://doi.org/10.1016/S1003-6326\(11\)61598-7](https://doi.org/10.1016/S1003-6326(11)61598-7)
  10. Patel V, Sali A, Hyder J, Corliss M, Hyder D, Hung W (2020) Electron beam welding of Inconel 718 electron beam welding of Inconel 718. In: *Procedia Manufacturing*. Elsevier B.V., 428–435
  11. Deng D, Peng RL, Brodin H, Moverare J (2018) Microstructure and mechanical properties of Inconel 718 produced by selective laser melting: sample orientation dependence and effects of post heat treatments. *Mater Sci Eng A* 713:294–306. <https://doi.org/10.1016/j.msea.2017.12.043>
  12. Ströbner J, Terock M, Glatzel U (2015) Mechanical and microstructural investigation of nickel-based superalloy IN718 manufactured by selective laser melting (SLM). *Adv Eng Mater* 17:1099–1105. <https://doi.org/10.1002/adem.201500158>
  13. Wang X, Chou K (2019) The effects of stress relieving heat treatment on the microstructure and residual stress of Inconel 718 fabricated by laser metal powder bed fusion additive manufacturing process. *J Manuf Process* 48:154–163. <https://doi.org/10.1016/j.jmapro.2019.10.027>
  14. Raza T, Andersson J, Svensson LE (2018) Vareststraint weldability testing of additive manufactured alloy 718. *Sci Technol Weld Join* 23:606–611. <https://doi.org/10.1080/13621718.2018.1437338>
  15. Xia C, Zhao M, Sun W, Li H, Liu P (2018) microstructure and properties of 3D printed Inconel 718 joint brazed with BNi-2 amorphous filler metal. *Mater Res* 22:1–10. <https://doi.org/10.1590/1980-5373-MR-2018-0348>
  16. Nahmany M, Rosenthal I, Benishti I, Frage N, Stern A (2015) Electron beam welding of AlSi10Mg workpieces produced by selected laser melting additive manufacturing technology. *Addit Manuf* 8:63–70. <https://doi.org/10.1016/j.addma.2015.08.002>
  17. Yu H, Li F, Yang J, Shao J, Wang Z, Zeng X (2018) Investigation on laser welding of selective laser melted Ti-6Al-4V parts: Weldability, microstructure and mechanical properties. *Mater Sci Eng A* 712:20–27. <https://doi.org/10.1016/j.msea.2017.11.086>
  18. Casalino G, Campanelli SL, Ludovico AD (2013) Laser-arc hybrid welding of wrought to selective laser molten stainless steel. *Int J Adv Manuf Technol* 68:209–216. <https://doi.org/10.1007/s00170-012-4721-z>
  19. Prashanth KG, Damodaram R, Scudino S, Wang Z, Prasad Rao K, Eckert J (2014) Friction welding of Al-12Si parts produced by selective laser melting. *Mater Des* 57:632–637. <https://doi.org/10.1016/j.matdes.2014.01.026>
  20. Popovich VA, Borisov EV, Popovich AA, Sufiarov VS, Masaylo DV, Alzina L (2017) Impact of heat treatment on mechanical behaviour of Inconel 718 processed with tailored microstructure by selective laser melting. *Mater Des* 131:12–22. <https://doi.org/10.1016/j.matdes.2017.05.065>
  21. Janaki Ram GD, Venugopal Reddy A, Prasad Rao K, Madhusudhan Reddy G (2005) Microstructure and mechanical properties of Inconel 718 electron beam welds. *Mater Sci Technol* 21:1132–1138. <https://doi.org/10.1179/174328405X62260>
  22. Khairallah SA, Anderson AT, Rubenchik A, King WE (2016) Laser powder-bed fusion additive manufacturing: Physics of complex melt flow and formation mechanisms of pores, spatter, and denudation zones. *Acta Mater* 108:36–45. <https://doi.org/10.1016/j.actamat.2016.02.014>

**Publisher's Note** Springer Nature remains neutral with regard to jurisdictional claims in published maps and institutional affiliations.